PCCP

PAPER

View Article Online
View Journal | View Issue

Cite this: *Phys. Chem. Chem. Phys.*, 2025, **27**, 14469

Origins of crystallisation-induced dual emission of terephthalic and isophthalic acid crystals†

Ljiljana Stojanović, *[ab] Michael Dommett [c] and Rachel Crespo-Otero *[d]

Metal-free organic crystals with room-temperature phosphorescence (RTP) present an innovative alternative to conventional inorganic materials for optoelectronic applications and sensing. Recently, substantial attention has been directed towards the design of new phosphorescent crystals through crystal engineering and functionalisation. In this paper, we investigate the excited-state deactivation mechanisms of two simple organic molecules: terephthalic acid (**TPA**) and isophthalic acid (**IPA**) using embedding models based on multiconfigurational MS-CASPT2 calculations. These molecules exhibit prompt and delayed fluorescence and RTP in the solid state. We explore intramolecular internal conversion pathways using high-level quantum chemistry methods in both solution and crystalline phases. We analyse deactivation mechanisms involving singlet and triplet states, quantifying direct and reverse intersystem crossing rates from the lowest triplet states, as well as fluorescence and phosphorescence rates. Additionally, our study examines singlet exciton transport in single crystals of **TPA** and **IPA**. Our findings clarify the mechanisms underlying the prompt and delayed fluorescence and RTP of crystalline **TPA** and **IPA**, revealing distinct differences in their deactivation processes. Notably, we explain the enhanced fluorescence and phosphorescence in **IPA** compared to **TPA**, emphasising how the positioning of the carboxylic group influences electronic delocalisation in excited states, (de)stabilising delocalised ππ* states along the reaction coordinate, thereby significantly impacting deactivation mechanisms.

Received 14th February 2025,
Accepted 16th June 2025

DOI: 10.1039/d5cp00603a

rsc.li/pccp

1 Introduction

Room-temperature phosphorescence (RTP) has generated significant interest among experimental and computational scientists due to its wide range of applications, including its use in highly emissive materials for organic light-emitting diodes (OLEDs), anti-counterfeiting, photovoltaic devices, and bioimaging.[1] Since efficient phosphorescence requires a substantial triplet population, these materials have traditionally been designed using inorganic and organometallic compounds that promote intersystem crossing (ISC) *via* strong spin–orbit coupling (SOC) and charge-transfer mechanisms. In contrast, organic molecules, due to their relatively small triplet populations and competing nonradiative pathways, typically exhibit phosphorescence only at cryogenic temperatures and under inert conditions in solution. However, recently RTP has been achieved in several purely organic crystals composed of molecules with relatively simple structures. These organic materials are significantly more cost-effective and environmentally friendly than their inorganic and organometallic counterparts.

Efficient triplet formation can be achieved in RTP organic crystals in compounds where the presence of heteroatoms facilitates intersystem crossing rates between relevant singlet and triplet states.[2] A second requirement for organic RTP is to establish a restrictive crystalline environment that suppresses large-amplitude molecular vibrations and reduces the rate of internal conversion to the ground state *via* conical intersections[3] or vibrational wavefunction overlaps.[4] Depending on the energy gaps and SOCs, RTP can compete with both prompt fluorescence (PF) and delayed fluorescence (DF).[5] DF can occur through reverse intersystem crossing (rISC), which is crucial in thermally activated delayed fluorescence (TADF) chromophores.[6]

Two of the simplest organic crystals exhibiting RTP are the two isomers of benzenedicarboxylic acid in the crystalline phase: terephthalic acid (**TPA**) and isophthalic acid (**IPA**).[7,8] These isomers differ in the relative positions of their substituents (Fig. 1). Transient photoluminescence spectroscopy of **TPA** and **IPA** in ethanol solution and disordered amorphous states

[a] *Department of Physics and Astronomy, University College London, London WC1E 6BT, UK. E-mail: ljiljana.stojanovic@stfc.ac.uk*
[b] *Hartree Centre, Science and Technology Facilities Council, Daresbury Laboratory, Daresbury, WA4 4AB, UK*
[c] *School of Physical and Chemical Sciences, Queen Mary University of London, London, E1 4NS, UK*
[d] *Department of Chemistry, University College London, 2020 Gordon St., London WC1H 0AJ, UK. E-mail: r.crespo-otero@ucl.ac.uk*

† Electronic supplementary information (ESI) available. See DOI: https://doi.org/10.1039/d5cp00603a

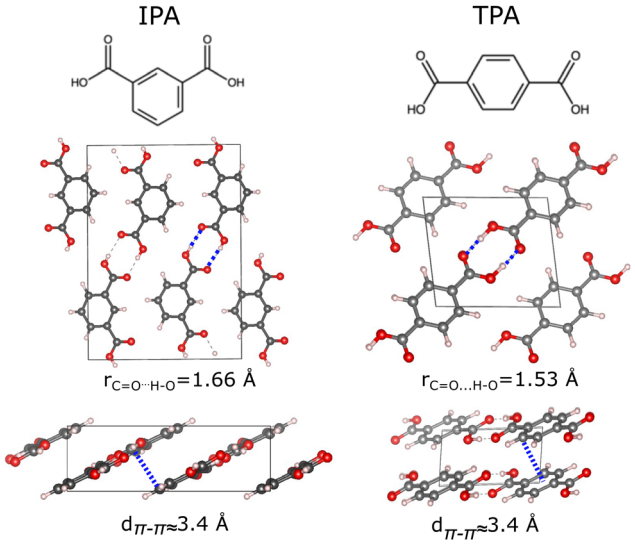

Fig. 1 Structures of **IPA** and **TPA** molecules (upper panel). The crystal structures of of **IPA** and **TPA** crystals, with designated unit cells, are represented in two different perspectives in the bottom panels.

reveals negligible luminescence quantum yields (below 0.6%). Upon crystallisation, both crystals exhibit dual emission, attributed to fluorescence and phosphorescence. The **TPA** crystal shows prompt deep blue emission at 388 nm with a lifetime of $\langle t \rangle$ = 0.53 ns and an emission efficiency of 8.4%. Additionally, a delayed fluorescence (DF) peak at 392 nm (slightly red-shifted compared to the prompt emission) and a shoulder at 511 nm, attributed to weak RTP, are observed. The experimental RTP lifetime is not determined on the millisecond timescale, suggesting longer lifetimes. The **IPA** crystal exhibits more efficient crystallisation-induced emission at 380 nm, with a quantum yield of 15.3%, attributed to prompt fluorescence. In addition to fluorescence, a long green afterglow lasting several seconds was observed, with distinct emission peaks at 384 nm and 506 nm, corresponding to DF and RTP, respectively. The measured lifetimes of prompt fluorescence, DF, and RTP in **IPA** are 1.81 ns, 9.6 ms, and 290 ms, respectively.[7]

Previous studies have investigated the mechanisms of fluorescence and phosphorescence in **TPA** and **IPA**.[7,9] Shuai *et al.* found the crystalline phase induces a change of ordering of the lowest-lying singlet and triplet states of **IPA** and **TPA** in comparison with the vacuum where the S_1 state is a $n\pi^*$, the higher $\pi\pi^*$ state becomes the lowest according to the CASSCF(8,8)/CASPT2/AMBER level of theory. This change induces higher luminescence yields and larger intersystem crossing rates in the crystal.[9] Gong *et al.* performed a similar optimisation of **TPA** and **IPA** in both the vacuum and crystalline phases based on QM/MM (TD-M06-2x/UFF) computations. They found that the energy gap between the closest-lying S_1 and T_2 states decreases while the spin–orbit coupling simultaneously increases in the crystal compared to the vacuum, leading to higher populations of the triplet state in the crystalline environment.[7] Here, we evaluate the impact of using different levels of theory on predicting the ordering of states and consider the competition between various radiative and non-radiative mechanisms.

While some aspects of the luminescence of **TPA** and **IPA** have been explored both experimentally and computationally, the precise mechanisms of excited state relaxation in solution and the crystalline phase have yet to be fully understood. There are still many open questions about the competition between different nonradiative and radiative decay pathways and the origin of DF. Our study aims to fill this gap by systematically investigating the molecule-centred excited state relaxation pathways using high-level computational methods. In addition to these pathways, we also analyse the dimer-centred mechanisms and exciton transport mechanisms in both crystal environments. Our calculations provide critical insights into the excited state relaxation mechanisms of **TPA** and **IPA**, enhancing the current understanding of their behaviour in solution and crystalline phases.

2 Computational details

We evaluated the performance of several methods for predicting excited states in **IPA** and **TPA** across vacuum, solution, and crystal environments. First, we optimised the ground states using the DFT method with B3LYP, PBE0, and ωB97XD functionals, and then computed the vertical excitations of the first five singlet and triplet states with the time-dependent DFT (TD-DFT) method[10–14] at the corresponding ground state minima. We also explored the resolution of identity coupled cluster method to the second order (RI-CC2)[15–18] and the multi-state complete active space second-order perturbation theory[19–21] ((MS-)CASPT2/CASSCF(14,11)) with the aug-cc-pVDZ basis set for describing the lowest-lying singlet and triplet states. For the RI-CC2 calculations, the ground state geometries were optimised at the CC2 level of theory, while for the CASPT2 computations, the ωB97XD/aug-cc-pVDZ ground state geometries were used. Solvent effects were considered by applying the polarisable continuum model (PCM) in the (TD-)DFT and CASPT2/CASSCF calculations, while the conductor-like screening model (COSMO) was used in the RI-CC2 computations. Ethanol was chosen as the solvent to facilitate comparison with available experimental results (dielectric permittivity ε_r = 24.55).

The performance of the excited state methods for the prediction of vertical excitations in the crystal environment was evaluated using QM/MM techniques. To represent the crystal environment, we first refined the experimental crystal structures of **TPA** and **IPA** (retrieved from the Cambridge Crystallographic Database, with CCDC codes 1269122 for **TPA**[22] and 1108748 for **IPA**[23]) by performing periodic boundary condition DFT calculations as implemented in Quantum Espresso.[24] The PBE-D2 functional, including a dispersion correction, was employed with a plane-wave cutoff of 30 Ry and a Monkhorst–Pack *k*-point grid of (1 × 2 × 1), chosen based on the unit cell shape. The projector augmented wave (PAW) pseudopotential was used to model the nuclei and core electrons, while the valence electrons were treated explicitly.[25,26] The optimisations

were carried out by relaxing the structure within the unit cell while keeping the cell dimensions fixed at their experimental values. Clusters consisting of 123 **TPA** and 120 **IPA** molecules (2214 and 2160 atoms, respectively) were extracted from the optimised supercells. The QM/MM simulations included one or two central molecules in the QM region, with the surrounding molecules treated using MM. The QM region was relaxed, while the MM region remained fixed at its optimised lattice positions. For TD-DFT optimisations in the solid state, the ONIOM(QM:MM)method[27,28] was applied, with the QM region treated at the (TD-)ωB97XD/6-311G(d,p) level of theory. For MS-CASPT2/CASSCF(14,11)/aug-cc-pVDZ calculations in the solid state, the QM/MM simulations were performed using the Molcas code for the electrostatic embedding QM calculations and the Tinker code for the MM part considering CM5 point charges. In the (TD-)DFT calculations, the MM region was described using the OPLS-AA force field, with ESP and CM5 charges derived from HF/3-21G calculations on a single molecule. The RI-CC2/aug-cc-pVDZ calculations were done only using electrostatic embedding with CM5 charges. While the calculations with TDDFT and CC2 methods were done using the geometries optimised with the same method, MS-CASPT2 calculations considered the ωB97XD/6-311G(d,p) ground-state structures. All (TD-)DFT computations were performed with the Gaussian 16 program,[29] CASSCF and CASPT2 computations with the Molcas code,[30] and RI-CC2 computations were performed with the Turbomole v7.0 code.[31]

To investigate the excited state relaxation mechanisms in solution and crystal phase, we optimised the excited states minima (S_1, T_1, T_2) and S_1–S_0 and T_1–S_0 minimum energy crossing points in both environments. The excited states (S_1, T_1, and T_2) were optimised at the CASSCF(14,11)/aug-cc-pVDZ level of theory because the TD-ωB97XD/6-311G(d,p) does not not predict correctly the types and ordering of all excited states of **TPA** and **IPA**. The S_1–S_0 minimum energy conical intersections (MECIs) optimisations were first carried out in solution and crystal phase at the SA-2-CASSCF(14,11)/6-31G(d) level of theory, using the branching plane update method[32] as implemented in Molcas code. The obtained S_1–S_0 MECI geometries are reoptimised at the extended multistate CASPT2 level (XMS-CASPT2).[33,34] The minimum energy crossing point between the ground and T_1 states was optimised based on T_1 states optimisation and S_0–T_1 energy gap criterion. In the solid state, the optimisations were done at the QM/MM level as described above.[30] The active spaces comprised of twelve π orbitals and 2p-orbitals of carboxyl group oxygen atoms for **IPA** and **TPA** (Fig. S1, ESI†), were used in all optimisations and single point computations. The single-point CASPT2 computations were based on configuration state functions obtained at the SA-6-CASSCF(14,11)/aug-cc-pVDZ level.[35] They were done without an IPEA shift and applying an imaginary shift of 0.1 a.u., which improves the convergence in the case of possible intruder states.[36]

Linearly interpolated pathways (LIIC) between S_0 and S_1–S_0 MECI geometries in the solution and crystal were created and six lowest-lying singlet and triplet excited states were computed at the MS-6-CASPT2/CASSCF(14,11)/aug-cc-pVDZ level at the obtained geometries. The spin–orbit couplings (SOCs) between relevant singlet and triplet states were computed at the excited states minima in solution and crystal and along the LIIC pathway in the crystal, as implemented in the Molcas code. The method relies on the computation of matrix elements of one-electron spin–orbit part of the Hamiltonian in the atomic mean field approximation[37,38] in the basis of the CASSCF wave functions. The SOCs between singlet and triplet pairs are obtained from the computed components corresponding to transitions between a singlet and three spin triplet components defined with quantum numbers $m_l \in \{-1, 0, 1\}$ as $|\langle S_a|H_{SO}|T_b\rangle| = \sqrt{\sum_{m_l\in-1,0,1}\langle S_a|H_{SO}|T_{m_l b}\rangle^2}$.

Furthermore, to examine the effect of hyperfine interactions between singlet and triplet states on the excited-state deactivation mechanisms (in particular on the reverse intersystem crossing), we computed the hyperfine Hamiltonian matrix between excited states,[39] as implemented in the Q-Chem program package.[40] The matrix elements of the complete hyperfine Hamiltonian, including spin–spin dipole, Fermi contact, and orbital response term are evaluated in the basis of the TD-DFT excited states.[39] The excited-states were computed with the ωB97XD functional and aug-cc-pVDZ basis set.

To investigate the dimer-centred relaxation mechanisms in the crystal phase, we optimised the S_0 and S_1 geometries of the dimers with the shortest centroid distances (π–π stacked dimers) applying the QM/QM′ approach as implemented in the fromage code.[41,42] The QM (dimer) is represented by the algebraic diagrammatic construction ADC(2)[43,44]/aug-cc-pVDZ method and QM′ (environment) region was simulated at the second order (SCC-)DFTB method, employing the mio-1-1 set of Slater–Koster parameters parametrised for the tight-binding SCC-DFTB Hamiltonian.[45,46] For the point charges in the environment, we used the ESP charges obtained at ωB97XD/6-31G(d) and PBE/6-31G(d) levels of theory, respectively. The DFTB calculations were performed with the DFTB+ program,[45] and the ADC(2) computations with the Turbomole program. The lowest lying singlet and triplet states of the optimised dimers were computed at the ADC(2)/aug-cc-pVDZ level of theory.

We estimated the fluorescence and phosphorescence rates in vacuum and crystal applying Fermi's golden rule for the transition between initial (i) and final state (f) states:

$$k_{if} = \frac{\eta^2 \Delta E^3}{3\varepsilon_0 \pi \hbar^4 c^3} |\langle \Psi_i|\hat{\mu}|\Psi_f\rangle|^2, \quad (1)$$

where ΔE is the vertical energy difference between states, ε_0 is the vacuum permittivity, $\hbar$ is reduced Planck constant, c is the speed of light in vacuum, η is the refractive index of the medium (1.51 for **TPA**) and $\hat{\mu}$ is the electric transition dipole moment operator. The expectation values of this operator are computed between eigenstates of the Hamiltonian including the spin–orbit term as implemented in Molcas, allowing to estimate the transition dipole moments between the ground state and singlet and triplet excited states.

The rates of the nonradiative electron transport (ET) processes (ISC, rISC and exciton transport) are estimated applying the Marcus semiclassical theory in the Condon approximations as

$$k_{\mathrm{ET}} = \frac{2\pi}{\hbar}|H_{ab}|^2 \frac{1}{\sqrt{4\pi\lambda k_{\mathrm{B}}T}} \exp - \left(\frac{\left(\Delta G^0 + \lambda\right)^2}{4\lambda k_{\mathrm{B}}T} \right), \qquad (2)$$

where T is the absolute temperature, k_{B} is the Boltzmann constant, λ is the reorganisation energy and ΔG^0 is the change of the adiabatic Gibbs free energy during the ET process. H_{ab} is the electronic coupling term between the diabatic states involved in the process. The term $F_k = \frac{1}{\sqrt{4\pi\lambda_{ab}k_{\mathrm{B}}T}} \exp - \left(\frac{\left(\Delta G^0 + \lambda\right)^2}{4\lambda k_{\mathrm{B}}T} \right)$ represents the vibrational density of states in the final state at the geometry of the initial state weighted by Franck–Condon factors in the limit of high temperatures.[47]

The reorganisation energy for (r)ISC was computed as $\lambda_{ab} \approx E_{\mathrm{T}_b}(\mathbf{R}_{\mathrm{minS}_a}) - E_{\mathrm{T}_b}(\mathbf{R}_{\mathrm{minT}_b})$ for the ISC and $\lambda_{ab} \approx E_{\mathrm{S}_b}(\mathbf{R}_{\mathrm{minT}_a}) - E_{\mathrm{S}_b}(\mathbf{R}_{\mathrm{minS}_b})$ for rISC (for clarification, for example $E_{\mathrm{T}_b}(\mathbf{R}_{\mathrm{minS}_a})$ is the energy of the T_b state evaluated at the minimum of the S_a state). The H_{ab} couplings correspond to the SOCs computed as described above. For the energy difference between the states (ΔE_{ab}) we used the difference between the energies of adiabatic states at the geometry at which the rates are computed ($\Delta E_{ab} = \Delta E_{ab}^{ad}$). The estimation of (r)ISC rates is done based on the MS-6-CASPT2/CASSCF(14,11)/aug-cc-pVDZ energies and CASSCF(14,11)/aug-cc-pVDZ spin–orbit couplings. We note that the energy gaps between singlet and triplet states correlate with the exchange interaction between those states, *i.e.* stronger exchange correlation induces larger gaps (ESI,† Section S2), and decreases the intersystem crossing rate. For this reason, an adequate treatment of electronic correlation using a high-level multiconfigurational methods, like CASPT2, is often necessary for the reliable prediction of ΔE_{ST} and consequently of the ISC rates.

In the case of exciton transport, the $\Delta E_{ab}^{ad} = 0$ as the exciton hopping occurs between donor and acceptor molecules with identical geometries. The intramolecular reorganisation energy induced by the exciton transfer (λ_{ab}) is computed considering one molecule (M_1) going from the fully relaxed ground state S_0 to the electronically excited state S_1 and a neighboring molecule (M_2) evolving in the opposite way as

$$\lambda_{\mathrm{exc}} = \lambda_{\mathrm{S}_1}^{M_1} + \lambda_{\mathrm{S}_0}^{M_2}. \qquad (3)$$

The exciton couplings ($H_{ab} = J_{ab}$) mediate the exciton transport process between the diabatic states (eqn (2)). The exciton transport rates are computed for the dimers with the centroid distances smaller than 10 Å, isolated from the optimised crystal structures. The J_{ab} of isolated dimers were computed applying a diabatisation method based on the transition dipole moments of S_1 states of isolated molecules and S_1 and S_2 states of dimers,[48] as implemented in the fromage code.[41] This method takes into account the short-range (exchange, orbital overlap, charge-transfer) and long-range Coulomb interactions. Both reorganisation energies for the exciton transport and exciton couplings are computed based on the TD-ωB97XD/6-311+G(d,p) excited states.

3 Results and discussion

3.1 Light absorption and emission

3.1.1 Vacuum and solution. The performance of several single-reference and multi-reference methods for the description of **TPA** and **IPA** excited states in vacuum, ethanol solution, and crystal phase is examined. The five lowest-lying singlet and triplet states of both molecules are computed by applying the TDDFT (with B3LYP, PBE0, and ωB97XD functionals), RI-CC2, and MS-CASPT2 methods at the ground state geometries optimised at the same level of theory. The excitation energies, oscillator strengths and types of states in vacuum/solution and crystal phase are given in Tables 1 and 2, the reported characters correspond to the MS-CASPT2 excited states. The excitations computed at other levels of theory were reordered to match the MS-CASPT2 excited states. In a few cases, the natures of the highest-lying excitations computed with the TD-DFT and RI-CC2 methods differ from the MS-CASPT2 ones, as highlighted in the comments in Tables 1 and 2. The transition densities are shown in the ESI† (Section S3).

We first compare the performance of three functionals, B3LYP, PBE0, and ωB97XD, for the prediction of excited states in vacuum. The bright S_4 state energies in vacuum computed applying these functionals deviate from each other by less than 0.3 eV in both molecules, whereas the energies of other states are predicted to be higher at the TD-ωB97XD level. The calculations with TD-ωB97XD show that, when using the PCM model for ethanol, the energies are shifted by approximately 0.1–0.3 eV, except for the highest singlet state considered (S_5), where the shift exceeds 0.5 eV. In Table 1, the vertical excitations obtained with RI-CC2 and MS-CASPT2 were calculated considering ethanol as the solvent, using the COSMO and PCM approaches, respectively. Comparing the excited state energies in the solution, we notice that the MS-CASPT2 S_1 ππ* state has ∼1 eV and 0.6 eV lower energy compared to the TD-ωB97XD and RI-CC2 energies, respectively. The dark nπ* states (S_2 and S_3) energies are overestimated for ∼0.5 eV at the TD-ωB97XD level, whereas the RI-CC2 predicts their excitation energies closer to the MS-CASPT2 values.

The experimental absorption spectra in ethanol of **TPA** and **IPA** featured two bands,[7] at 200 nm (6.20 eV) and 240 nm (5.17 eV) for **TPA** and at 210 nm (5.90 eV) and 230 nm (5.39 eV) for **IPA**. In the case of **TPA**, the MS-CASPT2/PCM reproduces well the first and second bright excitations at 4.92 eV and 6.16 eV. The TD-ωB97XD/PCM and RI-CC2/COSMO methods overestimate the energies of the bright singlet states and triplet excitations. The MS-CASPT2/PCM method reproduces well the first two bright excitations, the computed vertical excitation energies of bright S_4 and S_5 states are 5.20 eV and 5.34 eV in **IPA**, assignable to the first peak in the absorption spectrum with the maximum at 5.39 eV. The higher bright states contributing to the second absorption peak at 5.90 eV are not

Table 1 Vertical excitation energies (eV) and oscillator strengths (in parentheses) of the first five singlet and triplet states of **TPA** and **IPA** molecules in vacuum computed at several levels of theory. The 6-311+G(d,p) basis set was used in all DFT calculations, whereas the aug-cc-pVDZ set was used in RI-CC2 and CASPT2(14,11) computations

	B3LYP	PBE0	ωB97XD	ωB97XD/PCM	RI-CC2/COSMO	CASPT2/PCM	Exp.
TPA							
S_1 (ππ*)	4.52 (0.02)	4.67 (0.03)	4.84 (0.04)	4.98 (0.03)	4.56 (0.02)	4.02 (0.04)	
S_2 (nπ*)	4.51 (0.00)	4.67 (0.00)	5.06 (0.00)	5.30 (0.00)	4.76 (0.00)	4.80 (0.00)	
S_3 (nπ*)	4.57 (0.00)	4.73 (0.00)	5.11 (0.00)	5.32 (0.00)	4.80 (0.00)	4.88 (0.00)	
S_4 (ππ*)	5.02 (0.43)	5.16 (0.43)	5.33 (0.41)	5.52 (0.12)	5.39 (0.55)	4.92 (0.44)	5.17[c]
S_5 (ππ*)	6.20 (0.00)	6.44 (0.00)	6.72 (0.15)	6.01 (0.84)	6.71 (0.14)	6.16 (0.08)	6.20[c]
T_1 (ππ*)	3.26	3.18	3.33	3.44	3.73	3.36	
T_2 (ππ*)	3.68	3.75	3.94	4.20	4.24	3.97	
T_3 (ππ*)[b]	4.46	4.46	4.62	4.48	4.78	4.07	
T_4 (nπ*)[b]	4.17	4.27	4.65	4.89	5.63	4.69	
T_5 (nπ*)[b]	4.23	4.33	4.70	4.90	5.82	4.76	
IPA							
S_1 (ππ*)	4.72 (0.02)	4.87 (0.02)	5.01 (0.02)	4.79 (0.05)	4.68 (0.01)	3.94 (0.005)	
S_2 (nπ*)	4.77 (0.00)	4.91 (0.00)	5.21 (0.00)	5.12 (0.00)	4.92 (0.00)	4.60 (0.00)	
S_3 (nπ*)	4.80 (0.00)	4.94 (0.00)	5.23 (0.00)	5.18 (0.00)	4.94 (0.00)	4.61 (0.00)	
S_4 (ππ*)	5.32 (0.09)	5.46 (0.09)	5.60 (0.09)	5.24 (0.50)	5.70 (0.12)	5.20 (0.09)	
S_5 (ππ*)	5.48[a] (0.00)	5.76[a] (0.00)	6.20 (0.75)	6.74 (0.00)	6.12 (0.84)	5.34 (0.82)	5.39[c]
T_1 (ππ*)	3.40	3.29	3.43	3.33	3.88	3.06	
T_2 (ππ*)	3.99	4.05	4.22	3.91	4.45	3.64	
T_3 (ππ*)	4.22	4.28	4.50	4.62	4.61	4.04	
T_4 (nπ*)	4.39	4.47	4.78	4.72	4.68	4.33	
T_5 (nπ*)	4.41	4.50	4.80	4.78	5.41	4.37	

[a] S_5 states of IPA are predicted as nπ* at the B3LYP and PBE0 level. [b] T_3–T_5 states of TPA have different order at the B3LYP and PBE0 level. [c] Experimental excitation energies taken from ref. 7.

Table 2 Vertical excitation energies (eV) and oscillator strengths (in parentheses) of the first five singlet and triplet states of **TPA** and **IPA** molecules in crystal computed at several levels of theory. The 6-311+G(d,p) basis set is used in all DFT computations, whereas the aug-cc-pVDZ set is used in RI-CC2 and CASPT2(14,11) computations. the TD-ωB97XD results with the 6-31G(d) basis set are designated by asterix

	ωB97XD*	ωB97XD(CM5)	ωB97XD(ESP)	RI-CC2	CASPT2	Exp.
TPA						
S_1 (ππ*)	4.82 (0.04)	4.72 (0.04)	4.69 (0.04)	4.68 (0.03)	3.97 (0.08)	3.90[c]
S_2 (nπ*)	5.35 (0.37)	5.23 (0.42)	5.23 (0.42)	5.39 (0.00)	4.74 (0.29)	
S_3 (nπ*)	5.45 (0.00)	5.46 (0.00)	5.55 (0.00)	5.41 (0.12)	4.80 (0.00)	
S_4 (ππ*)	5.49 (0.04)	5.50 (0.01)	5.59 (0.01)	5.53 (0.42)	4.83 (0.07)	
S_5 (ππ*)	6.79 (0.00)	6.68 (0.00)	6.64 (0.00)	7.02[b] (0.00)	6.14 (0.38)	
T_1 (ππ*)	3.31	3.29	3.30	3.88	3.23	
T_2 (ππ*)	3.86	3.81	3.77	4.32	3.75	
T_3 (ππ*)	4.67	4.63	4.61	6.01	4.49	
T_4 (nπ*)	5.04	5.07	5.17	4.95	4.75	
T_5 (nπ*)	5.06	5.09	5.19	5.44	4.79	
IPA						
S_1 (ππ*)	5.08 (0.02)	4.98 (0.02)	4.96 (0.02)	3.69 (0.00)	3.93 (0.10)	4.00[c]
S_2 (nπ*)	5.56 (0.00)	5.53 (0.06)	5.52 (0.07)	4.13 (0.00)	4.57 (0.00)	
S_3 (ππ*)	5.72 (0.08)	5.56 (0.08)	5.56 (0.01)	4.17 (0.00)	5.26 (0.00)	
S_4 (ππ*/nπ*)	5.60[a] (0.01)	5.61[a] (0.02)	5.74 (0.01)	4.54 (0.00)	5.72 (0.18)	
S_5 (ππ*/nπ*)	6.31[a] (0.71)	6.10[a] (0.73)	6.08 (0.71)	4.66[b] (0.02)	5.97 (0.00)	
T_1 (ππ*)	3.46	3.43	3.44	3.68	3.29	
T_2 (ππ*)	4.27	4.19	4.20	4.00	3.85	
T_3 (ππ*)	4.54	4.47	4.46	4.08	3.96	
T_4 (nπ*)	4.99	4.89	4.88	4.15	4.47	
T_5 (nπ*)	5.13	5.14	5.26	4.36	5.11	

[a] S_4 and S_5 states of IPA show less nπ*/ππ* mixing according to the ωB97XD and RI-CC2 results, compared to the CASPT2 ones. They are predicted as ππ* at the ωB97XD level, and as nπ* and ππ* at the RI-CC2 level. [b] S_5 states of both IPA and TPA are predicted as nπ* at the RI-CC2 level. [c] Photon energies used in the photoexcitation spectra for **TPA** and **IPA** crystals as reported in ref. 8.

among the first five singlet states. These values are in very good agreement with the positions of the peak maxima (5.39 eV and 5.90 eV).

3.1.2 Crystalline phase. Table 2 presents the excitation energies obtained in the solid state. To assess the impact of using different point charges in the electrostatic embedding

with the TD-ωB97XD method, we performed calculations with both CM5 and ESP charges. The energy differences in all cases were smaller than or around 0.1 eV. Given this minor effect, the CASPT2 and CC2 calculations were conducted using only CM5 charges. As observed in solution (Table 1), the absorption energies of singlet states calculated with TD-ωB97XD and RI-CC2 in the crystal significantly deviate from those obtained with MS-CASPT2. For both **TPA** and **IPA**, TD-ωB97XD tends to overestimate the singlet energies. In contrast, RI-CC2 overestimates the singlet energies for **TPA** and underestimates them for **IPA**. However, the TD-ωB97XD and RI-CC2 energies for the low-lying triplet states are in relatively good agreement with the values from MS-CASPT2.

Table 3 shows the emission energies obtained after relaxation in S_1. While the MS-CASPT2 emission energies are close to the experimental emission maxima, deviating by only 0.3–0.4 eV, the TD-ωB97XD energies are overestimated by more than 1 eV. In contrast to the results reported by Ma *et al.*, we do not observe a change in the S_1 state type from ππ* to nπ* upon crystallisation in the Franck–Condon region.[9] According to our CASPT2 results, the S_1 states of **TPA** and **IPA** in vacuum, solution, and crystal phases possess ππ* character, while the higher S_2 and S_3 states exhibit nπ* character. However, we found that the nπ* state becomes the lowest-lying state along the internal conversion coordinate, as will be discussed below (Section 3.2). These differences from previous works are attributed to the different active spaces employed. Our CASSCF/CASPT2 simulations considered a [14,11] active space (9π and 2n orbitals), while the smaller[8,8] active space used in the work by Ma *et al.* comprised 6π and 2n orbitals. This suggests that including a larger number of π orbitals in the active space enabled the identification of a lower eigenvalue of the Hamiltonian, corresponding to the ππ* state, whereas the energies of two quasi-degenerate nπ* states are predicted to be very close at both levels of theory (approximately 4.8 eV, ref. 9 and Table 2).

Based on this benchmark, we conclude that the MS-CASPT2 method with the selected active space ([14,11]) reproduces the absorption and emission properties of **TPA** and **IPA** well (Table 3). In Section 3.2.1, we will present the deactivation pathways connecting the ground state minimum with the optimised minimal energy conical intersections (S_1–S_0 MECI). These pathways were obtained applying the MS-CASPT2 method, which, apart from the good performance in description of absorption and emission, is suitable for the excited states simulations in the vicinity of the conical intersection, due to multi-reference character of the wave function.

Table 3 Emission energies (eV) of the lowest-lying singlet state (S_1) in **TPA** and **IPA** molecules in crystal computed at the TD-ωB97XD/6-311+G(d,p) and CASPT2(14,11)/aug-cc-pVDZ levels of theory. Oscillator strengths are given in parentheses

	ωB97XD(CM5)	ωB97XD(ESP)	CASPT2	Exp.
TPA				
S_1 (ππ*)	4.40 (0.06)	4.28 (0.05)	3.61 (0.08)	3.20[a], 3.6[b]
IPA				
S_1 (ππ*)	4.70 (0.03)	4.68 (0.03)	2.96 (0.14)	3.26[a], 3.46[b]

[a] Experimental emission energies taken from the ref. 7. [b] Experimental emission energies taken from the ref. 8.

3.1.3 Crystal structure and exciton transport. The crystal structures of **TPA** and **IPA** crystals are given in Fig. 1. Both crystals are characterised by C═O···H–O hydrogen bonds between in-plane monomers. In the **TPA** crystal, each monomer is bonded with two C═O···H–O hydrogen bonds with the average length of 1.53 Å, creating linear chains of hydrogen bonded molecules. In the case of **IPA**, the zig-zag molecular chains are formed by C═O···H–O hydrogen bonds, with the average lengths of 1.66 Å. in both crystals, these chains create molecular planes with the distance of ∼3.4 Å, interacting with the adjacent planes through π···π interactions between molecules. The other O···H interactions between the molecules belonging to adjacent planes, between oxygen atoms from the C═O groups and hydrogen atoms from the C–H and O–H groups, have substantially larger lengths (between 2.5 and 2.7 Å[7]) and are weaker compared to the in-plane hydrogen bonds and π···π interactions.

To get an insight into intermolecular interactions and exciton transport mechanisms in **TPA** and **IPA** crystals, we isolated dimers from an optimised supercell with centroid distances smaller than 10 Å, and computed the exciton couplings between the lowest-lying bright states of monomers at the TD-ωB97XD/6-311+G(d,p) level. At this level of theory, the S_1 and S_2 states of monomers at the optimised crystal structures are quasi-degenerate and the exciton couplings are very small. The exciton coupling are computed between the bright S_2 (ππ*/nπ*) states, while the close-lying S_1 (nπ*) are dark states. The S_2 pairs of monomers combine in and form S_3 and S_4 states of isolated dimers. The dimers with the largest exciton couplings are the face-to-face slip-stacked dimers with the centroid distances ≈3.75 Å, interacting through π···π interactions between the π densities localised on phenyl rings and densities belonging to carboxylic groups (Fig. 2). Their interaction yields relatively weak couplings of 12 meV in both molecules. Other isolated dimers are mainly side-to-side dimers, including the dimers with the intermolecular C═O···H–O bonds, and have negligible exciton couplings (<5 meV). The reorganisation energies for the exciton transport computed using eqn (3) is 382 meV for **TPA** and 277 meV for **IPA**. Upon reorganisation from the FC region to the excited state minima, the transition density changes from mixed ππ*/nπ* at optimised crystal geometry (Fig. 2) to pure ππ* state in **TPA**, whereas in **IPA** the S_1 state has also a mixed ππ*/nπ* at its minimum (Fig. 6).

The exciton couplings are much smaller than the classical barrier for exciton hopping ($\lambda/4$), indicating that the S_1 excitons mostly remain localised on a single site during exciton diffusion in crystals. The exciton diffusion mechanism can be represented as a series of hopping events between isolated molecules. In this context, the exciton hopping rates for this mechanism can be evaluated based on the Marcus theory (eqn (2)). Applying the computed exciton couplings and reorganisation energies for **IPA** and **TPA**, the estimated exciton hopping rates for these molecules are 2.7×10^{10} and 8.3×10^{9} s^{-1}, respectively. This will compete

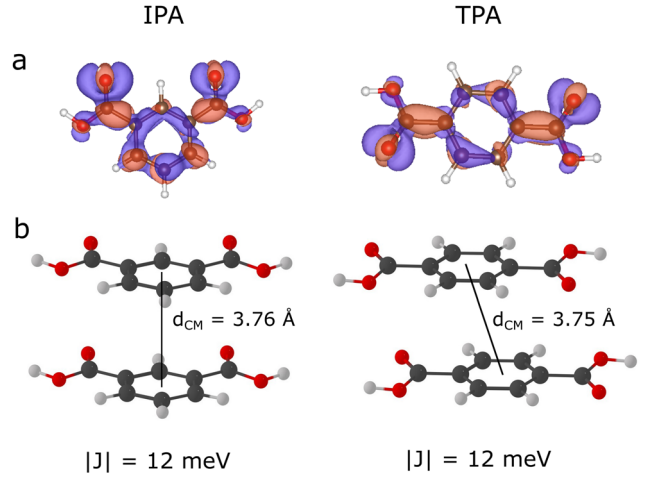

Fig. 2 TD-ωB97X-D/6-311+G(d,p) transition densities of the S_1 states of **IPA** and **TPA** computed at the optimised crystal geometry for an isolated molecule in vacuum (panel a). The isosurfaces corresponding to the 0.001 Å^3 density isovalue are represented. Structures of **IPA** and **TPA** dimers with the largest exciton couplings are presented in panel b. The electronic couplings and centre of masses distances between monomers are designated.

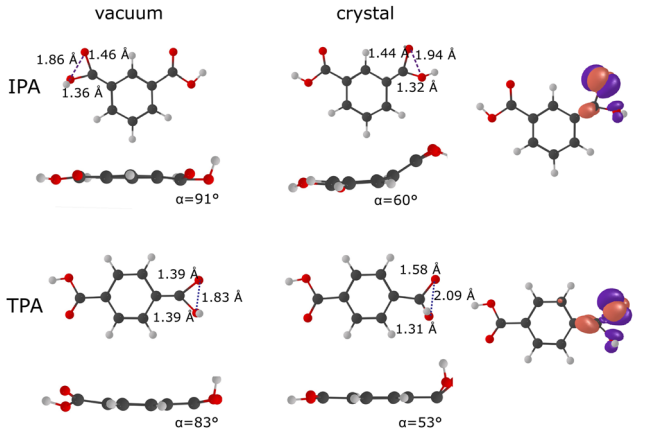

Fig. 3 Structures of conical intersections of **IPA** and **TPA** optimised at XMS-CASPT2[14,11]/6-31G(d) level in vacuum and crystal environment. The geometries are represented in top and side views. The lengths of the C–O bonds, distances between O atoms, and ∠HOCO dihedral angles (α) in the carboxyl group are designated.

with the vibrational relaxation to S_1 in the picosecond scale (rates around 10^{12} s^{-1}) followed by other processes such as fluorescence and ISC. Due to a smaller reorganisation energy, the exciton hopping rate in **IPA** are ∼4 times larger than in **TPA**. We note that the thermal effects, which can significantly affect the exciton couplings and exciton diffusion rates and mechanism, are neglected here.

3.2 Excited state mechanisms

In this section, we analyse different mechanisms associated with the excited state relaxation of **TPA** and **IPA**. Our main focus is understanding the competition of different pathways in the solid state.

3.2.1 S_1–S_0 MECI. To better understand nonradiative decay to the ground state, we examined the internal conversion processes for **TPA** and **IPA** molecules in ethanol and crystal phases. To examined the lowest energy internal conversion pathways, we optimised the S_1–S_0 minimum energy conical intersections (MECI) between S_0 and S_1 states in the solution and crystal phase (Fig. 3). All optimised S_1–S_0 MECI geometries correspond to the nπ* type structures with the additional deficiency of electronic density in from the p-orbital of O-atom from the OH-group. The conical intersection structure involves out-of-plane motions of carboxyl group proton and bond alternation of C═O and C_{Ph}–C_{Carb} bonds, *i.e.* the C═O bond elongates by ∼0.25 Å, while the C_{Ph}–C_{Carb} bond contracts by ∼0.15 Å with respect to the ground state values. Apart from this, the lone pair orbitals of oxygen atoms in carboxyl group rotate such that their axes lie in the COO-plane, and their interaction decreases their distance (by ∼0.2 Å) with respect to the standard distance. Similarly, ∠O═C–O angle decreases to 80–90° from 120°.

In the S_1–S_0 MECI structures optimised in the solution, the ∠HOCO is close to 90°, while the rest of the molecule is planar. On the other hand, in the solid state, the more favourable CI structures involve the bending of the COO-plane with respect to the rest of the molecule, while the H-atom dihedral motion is less activated (∠HOCO is 60° in **IPA** and 53.5° in **TPA**). A similar type of MECI structure was found in a phenyl-derivative dicarboxylic acid.[49]

The XMS-CASPT2 method is an appropriate choice for the optimisation of conical intersections, due to the multireference character of the wave function near these intersections. We also optimised the S_1–S_0 MECI using less computationally expensive single-reference methods, TD-DFT and ADC(2). These methods predicted the minimal energy crossing structures involving benzene ring puckering, which are much higher in energy compared to the CASPT2-optimised structures. Additionally, we optimised the S_1–S_0 MECI of dimers bonded through C═O···H–O hydrogen bonds at the TD-DFT and ADC(2) levels of theory to investigate whether internal conversion occurs through an intermolecular proton transfer mechanism. The obtained S_1–S_0 MECI structures involve geometry changes in only one of the molecules.

3.2.2 Nonradiative decay to S_0. Fig. 4 shows the PES of **IPA** and **TPA** along the internal conversion coordinate at CASPT2/SA-6-CASSCF(14,11)/aug-cc-pVDZ level of theory in the solid state. At the FC geometry, the oscillator strengths of S_1 ππ* increase compared to the values in solution (from 0.05 to 0.10 in **IPA** and from 0.04 to 0.08 for **IPA**). The second bright state of **IPA** in the crystal occurs at 5.72 eV, ∼0.4 eV above the bright state in the solution, while in the case of **TPA** the second bright state can be found at 4.74 eV, ∼0.45 eV below the bright excitation in the solution. The maximum excitation energy used in the experiment for both crystals is ∼3.5 eV (365 nm),[7] which corresponds to the first excited states (3.93 eV at the CASPT2 level, and 3.69 at the RI-CC2 level in **IPA** and 3.97 eV at the CASPT2 level in **TPA**).

The S_1–S_0 MECI for **IPA** lies at ∼5.2 eV, ∼1.2 eV above the vertical excitation, and for **TPA** at ∼6.0 eV, ∼2 eV above the

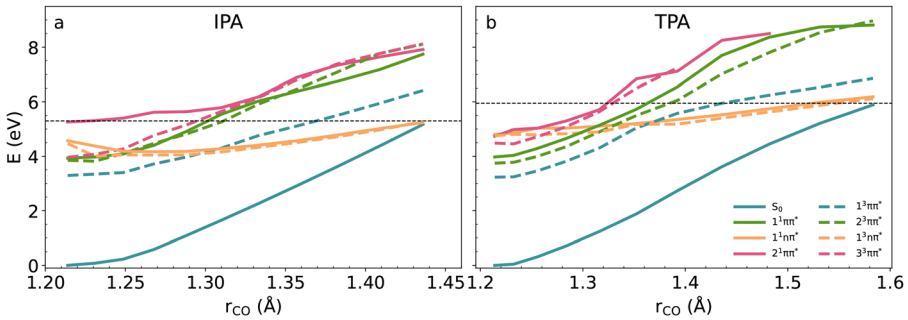

Fig. 4 CASPT2/SA-6-CASSCF(14,11)/aug-cc-pVDZ energies of the lowest-lying singlet and triplet states along the LIIC pathway connecting S_0 and MECI geometries in the crystal in **IPA** (panel a) and **TPA** (panel b) in a diabatic representation.

vertical excitation, and they are not classically accessible after the excitation to S_1 state. The excitation of the second bright state of **TPA** at 4.74 eV (S_2) would also not enable the internal conversion to the ground state. The excitation of high-energy bright states of **IPA** and **TPA** with energies close to 6 eV ($\sim$200 nm), would enable internal conversion, but that would require the application of vacuum UV radiation, not used in the experiment.[7] The crystal environment increases the energy barriers to the S_1–S_0 MECI with respect to solution in 0.4 eV for **IPA** and 0.8 eV for **TPA**. From the transition state theory, we can obtain that the fractions of nonradiative rates between the solid state and solution are in the order 10^{-7} for **IPA** and 10^{-14} **TPA** respectively. This is in line with the restricted access to the conical intersection (RACI) model, where the crystal environment blocks the access to the conical intersections associated with the S_1–S_0 nonradiative transitions explaining the enhancement of solid-state luminescence for these systems.[3,50,51] We should notice that for both S_1–S_0 MECI, T_1 gets almost degenerate with S_0 and S_1 providing an additional nonradiative pathway to the ground state, which can be activated by providing larger excitation energies.

The excitation to the S_1 state is followed by a relaxation to its minimum, where fluorescence and intersystem crossing can get activated. According to the PES and the spin–orbit couplings along the reaction coordinate (Fig. 4 and 5), the mechanisms involving triplet states are also possible. In the vicinity of the FC region, up to the (C=O) distance of $\sim$1.3 Å, where the T_1 and T_2 states are close-lying to the S_1, the S_1/T_1 and S_1/T_2 couplings have small values (below 5 cm^{-1}), indicating the possibility for slow intersystem crossing. The S_1/T_1 and S_1/T_2 SOCs values significantly increase further along the IC coordinate for $r_{CO} > 1.3$ Å, but in this region the S_1 state energy is higher than the vertical excitation, and the probability for its population *via* tunneling is relatively small.

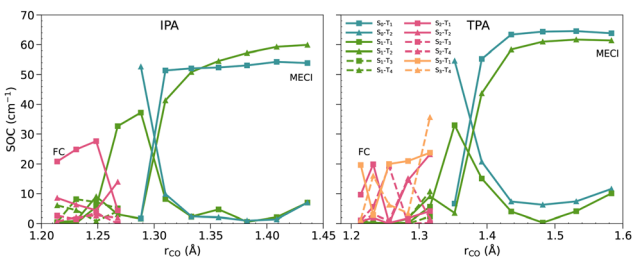

Fig. 5 Spin–orbit coupling matrix elements (SOC in cm^{-1}) between relevant adiabatic singlet/triplet excited states computed along the linearly interpolated pathways for nonradiative relaxation for **IPA** (left) and **TPA** (right) in the crystal. The couplings between the states with large energy gaps are not shown.

3.2.3 Prompt fluorescence. A fraction of the population of S_1 can decay to the ground state radiatively and both crystals show PF.[7] As mentioned in Section 3.1.2, the MS-CASPT2/aug-cc-pVDZ predicts well the values for fluorescence and emission energies. Using the Einstein equation, we estimated fluorescence rates of 1.7×10^8 and 9.9×10^7 s^{-1} for **IPA** and **TPA** corresponding to fluorescence lifetimes of 6 and 10 ns (Table 4). These values, particularly for **TPA**, are overestimated compared to the experimental values of 2 and 1 ns. This discrepancy might be related to the absence of excitonic effects in the calculations that could affect the oscillator strengths and the lack of consideration of vibrational effects.

3.2.4 Role of triplet states. To fully understand the mechanisms operating in these systems, we need to explore the role of triplet states in more detail. Our previous study showed that triplet states can be affected differently than singlet states in a solid-state environment.[52] Experimentally, in addition to PF, both systems show DF and RTP, which are directly linked with the population of triplet states. Fig. 6 shows the energy of the three lowest-lying singlet and triplet states computed at the optimised S_0, S_1, T_1, and T_2 geometries of **TPA** and **IPA** in crystal environment at the MS-CASPT2 level of theory. Possible decay pathways including radiative an nonradiative are highlighted in the figure, the details of the corresponding mechanisms are explained in the next sections. We note that the RI-CC2 method predicts similar excited state transition densities and energies at the (RI-)CC2 optimised

Table 4 Fluorescence (Fl), phosphorescence (Ph), most important (reverse) intersystem crossing (rISC) rate constants (k_f and k_P, $k_{(r)ISC}$, and k_{exc}) computed at 300 K in the **IPA** and **TPA** crystals. Section S7 in the ESI shows all calculated constants

	k_f (s^{-1})	k_P (s^{-1})	k_{ISC} (s^{-1})	k_{rISC} (s^{-1})
TPA	9.9×10^7	0.5	9.1×10^6 (S_1/T_4)	202 (T_3/S_2)
IPA	1.7×10^8	9.9	1.8×10^{11} (S_1/T_1)	523 (T_2/S_1)

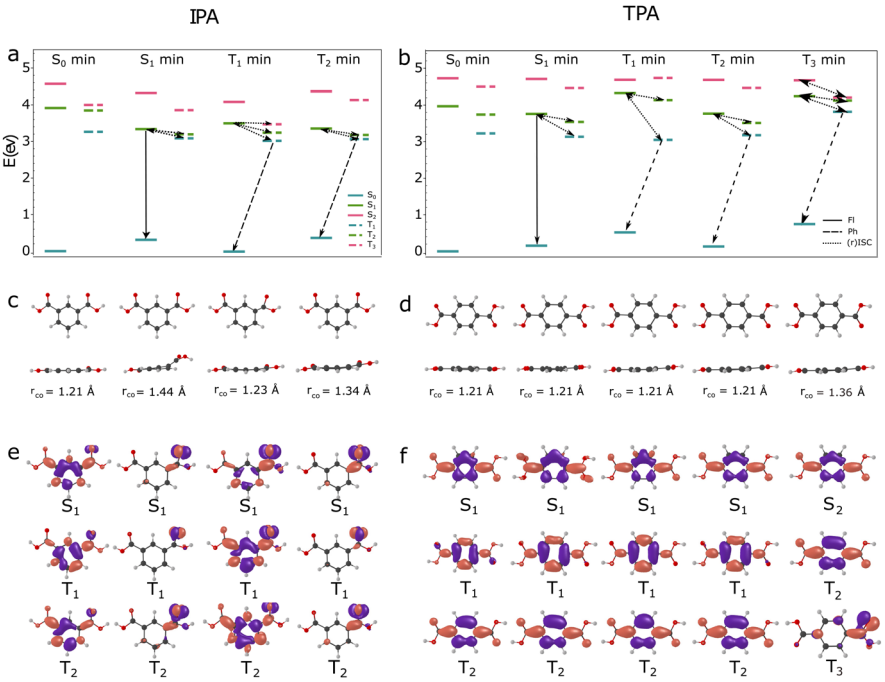

Fig. 6 Energy levels of the lowest-lying singlet and triplet states of **IPA** (panel a) and **TPA** (panel b) in crystal computed at the S_0, S_1, T_1, T_2, and T_3 (for **TPA**) states minima at the MS-CASPT2/CASSCF(14,11)/aug-cc-pVDZ level of theory. Possible fluorescence (full line), phosphorescence (dashed line), and (reversed) intersystem crossing (dotted line) transitions are designated. Optimised geometries of **IPA** (panel c) and **TPA** (panel d) molecules in S_0, S_1, T_1, T_2, and T_3 states given in two perspectives. The lengths of the C═O bond from the carboxylic group is given as well. The S_1, T_1, and T_2 excited state MS-CASPT2 density differences in the crystal environment are represented for **IPA** (panel e) and **TPA** (panel f) at S_0, S_1, T_1, and T_2 minima. In the case of the excited states of **TPA** at the T_3 minimum, the MS-CASPT2 density differences in the crystal environment are represented for S_2, T_2, and T_3 states.

geometries (ESI,† Section 8). According to the PES along the reaction coordinate which corresponds mainly to the C═O bond stretching, in both systems the lowest-lying excited states in the FC region are the ππ* states. They cross the higher nπ* singlet and triplet states at $r_{C=O} \sim 1.3$ Å in **IPA** and $r_{C=O} \sim 1.35$ Å in **TPA**. For the larger C═O lengths, the nπ* states become more stable (Fig. 5).

The most striking difference between **TPA** and **IPA** is related to the nature of the most stable excited states. In **IPA**, the lowest-lying excited states are nπ* states at the S_1 and T_2, and mixed nπ* and ππ* states at the T_1 geometry. Their geometries are non-planar, with signatures of distortions occurring at the conical intersection –C═O bond stretching and out-of-plane bending of carboxyl group with respect to the phenyl ring. In **TPA**, the lowest-lying S_1, T_1, and T_2 states are ππ* states. The geometries at their minima are planar structures and do not feature C═O elongation.

3.2.4.1 Intersystem crossing. We explore possible intersystem crossing mechanisms from the S_1 minima. In **TPA**, the energy gaps between S/T pairs (ΔE) at the S_1 geometry are 0.62 eV for the S_1/T_1 and 0.22 eV for the S_1/T_2 pair. Since these states are ππ* states, the spin–orbit couplings between S_1/T_1 is small (~ 4 cm^{-1}) and ~ 0 cm^{-1} for S_1/T_2 pair. The estimated ISC rates, based on the eqn (2), are negligible for the S_1/T_1 transition and zero ISC rate for the S_1/T_2 transition (Table 4, parameters used for the computations of all rates are given in the ESI†) at the S_1 geometry. The ISC S_1 (ππ*) and T_1/T_2 (ππ*) states are negligible along the reaction coordinate for the C═O lengths below 1.32 Å, as the gaps between states remain significant and spin–orbit couplings are close to zero. However, there is the possibility for the transition from the S_1 ππ* state to the higher-lying nπ* triplet state along the reaction pathway. The S_1 ππ* state crosses with the ^{3}nπ* triplet state at $r_{C=O} = 1.32$ Å. The minimum of the ^{3}nπ* state occurs at $r_{C=O} \approx 1.36$ Å (Fig. 6), after the crossing between ππ* and nπ* states along the reaction coordinate (Fig. 4). At this geometry, the ^{3}nπ* state (T_3) is 0.2 eV above the S_1 vertical excitation. The first two triplet states are ππ* states, whereas the first two singlet states are nπ* and ππ*, respectively. The calculated ISC rate for the $S_1/^3$nπ* transition at the minimum of the S_1 state is 1.6×10^5 s^{-1}. However, the spin–orbit couplings between these states increase along the reaction coordinate. The ISC rate computed applying the spin–orbit couplings in the vicinity of the crossing point between states ($r_{C=O} \approx 1.3$ Å) is 9×10^5 s^{-1}, indicating that a part of the population can be transferred to the ^{3}nπ* state, and subsequently to the lower-lying T_1 and T_2 ππ* states.

In **IPA**, two triplet states are in the vicinity of the S_1 state at its minimum (Fig. 6). The S_1 geometry features significant C═O stretching ($r_{C=O} = 1.44$ Å) and out-of-plane motions of carboxylic group (Fig. 6). As a consequence, the S_1, T_1, and T_2 states are nπ* states at this geometry. The S_1 and T_2 states are mostly represented by a single nπ* configuration, while the T_1

state is a linear combination of two nπ* configurations of opposite signs, inducing vanishing density around the C_{Ph}–C_{Carb} bond, and the total transition density is localised on C=O oxygen atom. Furthermore, the T_1 transition density is rotated for π/2 around the C=O bond with respect to the S_1 density. The T_2 density is also slightly rotated with respect to the S_1 density. These differences induce significant spin–orbit couplings between S_1/T_1 and S_1/T_2 pairs (32.4 and 27.2 cm^{-1}, respectively). Moreover, relatively small S–T gaps at this geometry (0.27 eV and 0.18 eV) enable significant ISC rates considerably faster than in **TPA**. The computed rates are 1.8 × 10^{11} s^{-1} for the S_1/T_1 transition and 9 × 10^6 s^{-1} for the S_1/T_2 transition (Table 4). Since the ISC rates to the T_1 state are larger compared to the fluorescence rates from the S_1 minimum ($k_f \approx$ 1.7 × 10^8 s^{-1}), a significant population transfer from the S_1 to T_1 state is expected. According to the reaction pathways (Fig. 4), the lowest-lying ππ* triplet states (T_1 and T_2 in the FC region) can be populated through internal conversion from the nπ* triplet state. This mechanism involves the planarisation of molecule and contraction of the C=O bond.

In both systems, the population transferred to the lowest-lying triplet states could deactivate through phosphorescence, ISC to the ground state, and reversed ISC to the singlet states.[5] According to the potential energy profiles along the reaction pathways, the ISC to the ground state is hindered in both systems, because the S_0/T_1 crossings, which are in the vicinity of the S_1–S_0 MECI (Fig. 6), are classically inaccessible following the S_1 excitations.

3.2.4.2 Room temperature phosphorescence. Once the T_1 states get populated, a possible relaxation mechanism is phosphorescence in both systems. Similar as fluorescence, the ultralong phosphorescence in **IPA** is more efficient compared to the **TPA**, with the computed rates of 9.92 s^{-1} and 0.5 s^{-1}, respectively. In **IPA**, according to our results, phosphorescence occurs at 2.91 eV with a lifetime of ∼100 ms. The available experimental phosphorescence energies and lifetimes are in relatively good agreement with our results; RTP is observed at 2.45 eV (506 nm) with a lifetime of 290 ms by Gong *et al.*,[7] and in the study by Kuno *et al.*[8] at 2.51 eV (501 nm). Our computations predict an ultralong phosphorescence at 2.53 eV for **TPA**, in good agreement with the experimental weak phosphorescence signal at 2.43 eV (511 nm) by Gong *et al.*[7] and at 2.40 eV (516 nm) by Kuno *et al.*[8]

3.2.4.3 Reverse intersystem crossing. To examine the deactivation pathways from the triplets populated from the singlet states through intersystem crossing, we optimised the geometries of the T_1 and T_2 states in both systems, and the T_3 state in **TPA**, and computed the reverse ISC rates from the minima of the triplet states. Because these systems experimentally exhibit DF, there must be mechanisms that efficiently populate S_1 from the triplet manifold. However, in both systems, population of singlet states from T_1 seems unlikely due to the significant energy gaps. Nevertheless, we observe that when considering higher triplet states, such as T_2 and T_3, the rates for rISC can be one to two order of magnitudes faster than competing phosphorescence. Previous works highlight the relevant role of the higher-lying triplets in the rISC mechanism in organic systems.[5,6,53–55] In cases where the energy gap between the T/S pair undergoing reverse ISC is substantial, intermediate triplet states can mediate this process. Vibronic interactions between closely spaced triplet states can promote internal conversion between them, effectively lowering the activation energy required for reverse ISC. Our hypothesis is that T_2 in **IPA** and T_3 in **TPA** lie very close in energy to T_1 and T_2, respectively, which should facilitate seamless population transfer between these states.

In **TPA**, the lowest T_1 and T_2 states at their minima are ππ* states. The computed rISC rates from the T_1 and T_2 state minima (the T_2 state is the lowest triplet state at its minimum) to the S_1 state are negligible (10^{-18} s^{-1}) at the T_1 minimum and zero at the (T_2 minimum), as a consequence of negligible/zero SOCs between (ππ*) states. To explain the rISC mechanism, we take into account the higher-lying 1^3nπ* state. At the minimum of this state (T_3), the lower-lying T_1 and T_2 states are ππ* states. The T_3 state can get populated due to excess vibrational energy obtained following the S_1/T_3 ISC. At this geometry, there is a possibility for the rISC to the higher-lying S_2 ππ* state (corresponding to the S_1 state at the FC region) from the T_3 (1^3nπ*) state, due to a significant SOC between the states (10 cm^{-1}). The computed rISC rate is ∼200 s^{-1}. The model used to compute the rISC rates (eqn (2)) does not take into account vibrational effects on spin–orbit interaction[56] and vibronic coupling between triplet states,[55] which could enhance the rISC rates. Another possible rISC mechanism at the T_3 geometry includes the transition from the ππ* T_1/T_2 states to the close-lying S_1 (nπ*) state. The T_2/S_1 rISC is expected to be efficient, since the ΔE is only ∼0.13 eV, while the T_2/S_1 SOC is 12.4 cm^{-1}. Moreover, the SOCs increase substantially along the reaction coordinate, surpassing 40 cm^{-1} for the $r_{C=O}$ > 1.38 Å (Fig. 5), which could further increase the rISC rates.

In **IPA**, the T_1 state minium has a planar geometry with slightly elongated C=O bond ($r_{C=O}$ = 1.23 Å) compared to the ground state geometry ($r_{C=O}$ = 1.21 Å) (Fig. 6). The S_1 state corresponds to the nπ*, whereas lower-lying T_1 and T_2 states correspond to the mixed nπ*/ππ* states at this geometry. The SOCs between the S_1 and T_1 states are 3 cm^{-1}. A significant S_1–T_1 gap at this geometry (0.71 eV), induces negligible rISC rate (Section S7 in the ESI†). The T_2 state features C=O stretching ($r_{C=O}$ = 1.34 Å) and out-of-plane motion of –COOH group. Similar as at the S_1 geometry, S_1, T_1, and T_2 states are nπ* states at this geometry. We note that the T_2 state is the second triplet state at its minimum. A significant SOC between S_1/T_1 pair (15.4 cm^{-1}) and a relatively small energy gap (0.18 eV) induce more efficient rISC from T_2 to the S_1 state with the rate of 523 s^{-1}, in comparison with the T_1/S_1 rISC. The T_2/S_1 rISC rates can increase along the stretching coordinate, as a results of an increase of the SOCs between them. Similar as for **TPA**, the T_2/S_1 SOCs significantly increase for $r_{C=O}$ > 1.3 Å, reaching the values of 50 cm^{-1} (Fig. 5). Based on this analysis, we can conclude that a part of the population from the triplet states

could be transferred back to the S_1 state in both **IPA** and **IPA** due to spin–orbit interactions between states.

Previous studies suggest that apart from the spin–orbit interactions, the hyperfine interactions between singlet/triplet pairs could contribute to the rISC mechanism, in particular in intermolecular processes in multi-chromophore systems involving radical-pair charge transfer states.[39,57] For the **IPA** crystal, Kuno *et al.*[8] found that the phosphorescence decreases upon Zeeman splitting of the degenerate triplet state in an external magnetic field and CH-to-CD substitution, but increases in stronger magnetic fields. This was explained by a charge-transfer (CT) state delocalised over two molecules, with spins localised on each, forming nearly degenerate singlet and triplet radical-ion-pair states. Weak hyperfine couplings enable spin exchange between them, accounting for both the suppression (Zeeman effect) and enhancement (Δg mechanism) of phosphorescence. We have explored the effects of hyperfine interactions on intramolecular mechanisms. In the case of the excited states of **TPA** and **IPA**, the hyperfine couplings between the singlet and triplet states, calculated using the TD-ωB97XD method, are negligible—less than 10^{-14} meV (see ESI,† Section S9). Consequently, the influence of hyperfine interactions on singlet–triplet mixing can be considered negligible, suggesting that reverse intersystem crossing (rISC) will be primarily facilitated by spin–orbit interactions. Additionally, our calculations using electrostatic embedded RI-ADC(2)/aug-cc-pVDZ method for the lowest-lying singlet and triplet states (S_1, S_2, T_1–T_4) for the dimers of **TPA** and **IPA** (ESI,† Section S10), indicated these states are either localised or delocalised nπ* and ππ* states, without a significant radical-ion pair charge transfer character.

3.2.4.4 Delayed fluorescence. Our results show that the rISC, activated in both systems, enables the transfer of a fraction of the population from triplet manifold to the S_1 states. A fraction of transferred population can undergo delayed fluorescence. In **IPA**, the delayed fluorescence is observed at 3.23 eV (slightly redshifted compared to the PF at 3.26 eV) with a lifetime of 9.6 ms.[7] Similarly, in **TPA** a weak DF signal is recorded at 3.16 eV (392 nm), slightly redshifted compared to the prompt signal (3.20 eV) with the 0.16 ms lifetime. The computed rISC rates in both crystals (k_{rISC} = 523 s^{-1} for T_2/S_1 transition in **IPA** and k_{rISC} = 202 s^{-1} for T_3/S_2 transition in **TPA**) indicate that the delayed fluorescence lifetime is expected on the ms timescale, which is in line with the experiments despite we are not considering the times associated with the transitions between the different triplets.

Kuno *et al.* attributed the delayed fluorescence observed in IPA to a triple–triplet annihilation (TTA) mechanism, in which two triplet excitons on neighbouring molecules combine to form one S_1 state and one S_0 state, with emission arising from the former.[8] To assess the thermodynamic feasibility of TTA, we evaluated the energy losses in both the singlet and triplet manifolds (ESI,† Section S11). Efficient TTA requires a small positive energy loss in the singlet states and a significantly negative loss in the triplet states.[47] However, our calculations reveal that energy losses in the singlet manifold are large and positive (for both S_1 and S_2 excitations), and those in the triplet manifold are also large and positive (ESI,† Section S11). These results suggest that the TTA mechanism is energetically unfavourable in these crystals.

4. Conclusions

Motivated by distinct solid-state luminescence properties of two benzene dicarboxyl acid crystals, **TPA** and **IPA**, we have systematically explored their excited-state relaxation mechanisms in solution and crystal environments. Given the weak interactions between π–π stacked dimers, the exciton couplings in both molecules are very small compared to the reorganisation energies associated with exciton transport. As a result, excited-state processes are primarily localised, and exciton transport occurs predominantly through incoherent exciton hopping.

We explore light-activated nonradiative decay mechanisms for both systems, considering multireference methods. We found the conical intersections geometries associated with the decay to the ground state, that involve mainly distortions of a carboxyl group –C═O bond stretching, out-of-plane motions of the carboxyl group with respect to the phenyl ring, and out-of-plane motion of the H-atom with respect to the –COO plane of carboxyl group. In line with the restricted access to the conical intersection (RACI) mechanism, the conical intersections in the crystal environment are not classically accessible. We also explore the intersystem crossing pathways in both systems, enabling relatively efficient populations of triplet states. In general, ISC is more efficient in **IPA** due to larger SOCs associated with the nature of the excited states involved and smaller energy gaps. We have shown that in both systems, the reverse intersystem crossing could happen through intermediate triplet states, transferring back a part of the population to the singlet manifold, explaining experimentally observed delayed fluorescence. This phenomenon is more efficient in **IPA**, due to a larger SOC and a smaller energy gap between states involved in the transition. According to our calculations, TTA seems to be energetically unfavourable.

Our results show that for an efficient triplet states population and solid-state phosphorescence in organic crystals, apart from the hindrance of the internal conversion, the positioning of substituents in benzene dicarboxylic acids plays a significant role. In the case of *para* substitution, the electronic delocalisation over the entire molecule is stabilised in the low-lying singlet and triplet states, resulting in ππ* being the lowest in energy. With *meta* substitution, electronic delocalisation is less favorable, leading to the stabilisation of mixed nπ*/ππ* or pure nπ* at their respective minima. This electronic effect significantly influences deactivation pathways. Our results indicate that the fluorescence, phosphorescence, and triplet-state population thought intersystem crossing processes are more efficient in **IPA**, which is in line with experimental observations. We believe this effect can be generalised to other substituents involved in electronic delocalisation with the central ring, as

well as to more complex conjugated systems. This result might be of interest for the design of highly efficient room-temperature phosphorescent materials.

Conflicts of interest

There are no conflicts to declare.

Data availability

The data supporting this article have been included as part of the ESI.†

Acknowledgements

This research was supported by the Leverhulme Trust (RPG-2019-122) and EPSRC (EP/R029385/1). We used the Queen Mary's Apocrita HPC facility, supported by QMUL Research-IT and UCL High Performance Computing Facilities Myriad@UCL and Kathleen@UCL. We also acknowledge the use ARCHER UK National Supercomputing Service (EP/X035859/1) *via* the Materials Chemistry Consortium and the Molecular Modelling Hub for computational resources, MMM Hub, which is partially funded by EPSRC (EP/T022213/1). Funding by the UK Research and Innovation under the UK government's Horizon Europe funding guarantee (grant number EP/X020908/2) is acknowledged.

Notes and references

1 W. Zhao, Z. He and B. Z. Tang, *Nat. Rev. Mater.*, 2020, **5**, 869–885.
2 J. Zhou, L. Stojanović, A. A. Berezin, T. Battisti, A. Gill, B. M. Kariuki, D. Bonifazi, R. Crespo-Otero, M. R. Wasielewski and Y. L. Wu, *Chem. Sci.*, 2021, **12**, 767–773.
3 R. Crespo-Otero, Q. Li and L. Blancafort, *Chem. – Asian J.*, 2019, **14**, 700–714.
4 Y. Niu, Q. Peng and Z. Shuai, *Sci. China, Ser. B: Chem.*, 2008, **51**, 1153–1158.
5 A. Sidat, F. J. Hernández, L. Stojanović, A. J. Misquitta and R. Crespo-Otero, *Phys. Chem. Chem. Phys.*, 2022, **24**, 29437–29450.
6 T. J. Penfold, F. B. Dias and A. P. Monkman, *Chem. Commun.*, 2018, **54**, 3926–3935.
7 Y. Gong, L. Zhao, Q. Peng, D. Fan, W. Z. Yuan, Y. Zhang and B. Z. Tang, *Chem. Sci.*, 2015, **6**, 4438–4444.
8 S. Kuno, H. Akeno, H. Ohtani and H. Yuasa, *Phys. Chem. Chem. Phys.*, 2015, **17**, 15989–15995.
9 H. Ma, W. Shi, J. Ren, W. Li, Q. Peng and Z. Shuai, *J. Phys. Chem. Lett.*, 2016, **7**, 2893–2898.
10 R. Bauernschmitt and R. Ahlrichs, *Chem. Phys. Lett.*, 1996, **256**, 454–464.
11 M. E. Casida, C. Jamorski, K. C. Casida and D. R. Salahub, *J. Chem. Phys.*, 1998, **108**, 4439–4449.
12 E. R. Stratmann, G. E. Scuseria and M. J. Frisch, *J. Chem. Phys.*, 1998, **109**, 8218–8224.
13 C. V. Caillie and R. D. Amos, *Chem. Phys. Lett.*, 1999, **308**, 249–255.
14 F. Furche and R. Ahlrichs, *J. Chem. Phys.*, 2002, **117**, 7433–7447.
15 O. Christiansen, H. Koch and P. Jørgensen, *Chem. Phys. Lett.*, 1995, **243**, 409–418.
16 C. Hättig and A. Köhn, *J. Chem. Phys.*, 2002, **117**, 6939–6951.
17 C. Hättig, *J. Chem. Phys.*, 2003, **118**, 7751–7761.
18 A. Köhn and C. Hättig, *J. Chem. Phys.*, 2003, **119**, 5021–5036.
19 B. O. Roos, A. J. Sadlej, P. Å. Malmqvist, K. Andersson and K. Wolinski, *J. Phys. Chem.*, 1990, **94**, 5483–5488.
20 K. Andersson, P. Å. Malmqvist and B. O. Roos, *J. Chem. Phys.*, 1992, **96**, 1218–1226.
21 S. Vancoillie, M. G. Delcey, R. Lindh, V. Vysotskiy, P.-Å. Malmqvist and V. Veryazov, *J. Comput. Chem.*, 2013, **34**, 1937–1948.
22 M. Bailey and C. J. Brown, *Acta Crystallogr.*, 1967, **22**, 387–391.
23 R. Alcala and S. Martnez-Carrera, *Acta Crystallogr., Sect. B*, 1972, **28**, 1671–1677.
24 P. Giannozzi, S. Baroni, N. Bonini, M. Calandra, R. Car, C. Cavazzoni, D. Ceresoli, G. L. Chiarotti, M. Cococcioni, I. Dabo, A. Dal Corso, S. De Gironcoli, S. Fabris, G. Fratesi, R. Gebauer, U. Gerstmann, C. Gougoussis, A. Kokalj, M. Lazzeri, L. Martin-Samos, N. Marzari, F. Mauri, R. Mazzarello, S. Paolini, A. Pasquarello, L. Paulatto, C. Sbraccia, S. Scandolo, G. Sclauzero, A. P. Seitsonen, A. Smogunov, P. Umari and R. M. Wentzcovitch, *J. Phys.: Condens. Matter*, 2009, **21**, 395–502.
25 P. E. Blöchl, *Phys. Rev. B: Condens. Matter Mater. Phys.*, 1994, **50**, 17953–17979.
26 G. Kresse and D. Joubert, *Phys. Rev. B: Condens. Matter Mater. Phys.*, 1999, **59**, 1758–1775.
27 S. Dapprich, I. Komaromi, K. Suzie Byun, K. Morokuma and M. J. Frisch, *J. Mol. Struct.: THEOCHEM*, 1999, **461–462**, 121.
28 L. W. Chung, W. M. Sameera, R. Ramozzi, A. J. Page, M. Hatanaka, G. P. Petrova, T. V. Harris, X. Li, Z. Ke, F. Liu, H. B. Li, L. Ding and K. Morokuma, *Chem. Rev.*, 2015, **115**, 5678–5796.
29 M. J. Frisch, G. W. Trucks, H. B. Schlegel, G. E. Scuseria, M. A. Robb, J. R. Cheeseman, G. Scalmani, V. Barone, G. A. Petersson, H. Nakatsuji, X. Li, M. Caricato, A. V. Marenich, J. Bloino, B. G. Janesko, R. Gomperts, B. Mennucci, H. P. Hratchian, J. V. Ortiz, A. F. Izmaylov, J. L. Sonnenberg, D. Williams-Young, F. Ding, F. Lipparini, F. Egidi, J. Goings, B. Peng, A. Petrone, T. Henderson, D. Ranasinghe, V. G. Zakrzewski, J. Gao, N. Rega, G. Zheng, W. Liang, M. Hada, M. Ehara, K. Toyota, R. Fukuda, J. Hasegawa, M. Ishida, T. Nakajima, Y. Honda, O. Kitao, H. Nakai, T. Vreven, K. Throssell, J. A. Montgomery, Jr., J. E. Peralta, F. Ogliaro, M. J. Bearpark, J. J. Heyd, E. N. Brothers, K. N. Kudin, V. N. Staroverov, T. A. Keith, R. Kobayashi, J. Normand, K. Raghavachari, A. P. Rendell, J. C. Burant, S. S. Iyengar, J. Tomasi, M. Cossi, J. M. Millam, M. Klene, C. Adamo, R. Cammi, J. W. Ochterski, R. L. Martin, K. Morokuma, O. Farkas, J. B. Foresman and D. J. Fox, *Gaussian~16 Revision A.03*, Gaussian Inc., Wallingford CT, 2016.
30 F. Aquilante, J. Autschbach, R. K. Carlson, L. F. Chibotaru, M. G. Delcey, L. De Vico, I. Fdez. Galván, N. Ferré, L. M.

Frutos, L. Gagliardi, M. Garavelli, A. Giussani, C. E. Hoyer, G. Li Manni, H. Lischka, D. Ma, P. Å. Malmqvist, T. Müller, A. Nenov, M. Olivucci, T. B. Pedersen, D. Peng, F. Plasser, B. Pritchard, M. Reiher, I. Rivalta, I. Schapiro, J. Segarra-Martí, M. Stenrup, D. G. Truhlar, L. Ungur, A. Valentini, S. Vancoillie, V. Veryazov, V. P. Vysotskiy, O. Weingart, F. Zapata and R. Lindh, *J. Comput. Chem.*, 2016, **37**, 506–541.

31 TURBOMOLE V7.0 2015, a development of University of Karlsruhe and Forschungszentrum Karlsruhe GmbH, 1989-2007, TURBOMOLE GmbH, since 2007; available from **https://www.turbomole.com**.

32 S. Maeda, K. Ohno and K. Morokuma, *J. Chem. Theory Comput.*, 2010, **6**, 1538–1545.

33 A. A. Granovsky, *J. Chem. Phys.*, 2011, **134**, 214113.

34 T. Shiozaki, W. Györffy, P. Celani and H.-J. Werner, *J. Chem. Phys.*, 2011, **135**, 081106.

35 B. O. Roos, P. R. Taylor and P. E. M. Siegbahn, *Chem. Phys.*, 1980, **48**, 157–173.

36 N. Forsberg and P. Å. Malmqvist, *Chem. Phys. Lett.*, 1997, **274**, 196–204.

37 P. Åke Malmqvist, B. O. Roos and B. Schimmelpfennig, *Chem. Phys. Lett.*, 2002, **357**, 230–240.

38 B. Schimmelpfennig, *Amfi, an atomic mean-field spin–orbit integral program. Computer code*, University of Stockholm, 1996.

39 S. R. May, C. Climent, Z. Tao, S. A. Vinogradov and J. E. Subotnik, *J. Phys. Chem. A*, 2023, **127**, 3591–3597.

40 Y. Shao, Z. Gan, E. Epifanovsky, A. T. Gilbert, M. Wormit, J. Kussmann, A. W. Lange, A. Behn, J. Deng, X. Feng, D. Ghosh, M. Goldey, P. R. Horn, L. D. Jacobson, I. Kaliman, R. Z. Khaliullin, T. Kuś, A. Landau, J. Liu, E. I. Proynov, Y. M. Rhee, R. M. Richard, M. A. Rohrdanz, R. P. Steele, E. J. Sundstrom, H. L. Woodcock III, P. M. Zimmerman, D. Zuev, B. Albrecht, E. Alguire, B. Austin, G. J. O. Beran, Y. A. Bernard, E. Berquist, K. Brandhorst, K. B. Bravaya, S. T. Brown, D. Casanova, C.-M. Chang, Y. Chen, S. H. Chien, K. D. Closser, D. L. Crittenden, M. Diedenhofen, R. A. DiStasio Jr., H. Do, A. D. Dutoi, R. G. Edgar, S. Fatehi, L. Fusti-Molnar, A. Ghysels, A. Golubeva-Zadorozhnaya, J. Gomes, M. W. Hanson-Heine, P. H. Harbach, A. W. Hauser, E. G. Hohenstein, Z. C. Holden, T.-C. Jagau, H. Ji, B. Kaduk, K. Khistyaev, J. Kim, J. Kim, R. A. King, P. Klunzinger, D. Kosenkov, T. Kowalczyk, C. M. Krauter, K. U. Lao, A. D. Laurent, K. V. Lawler, S. V. Levchenko, C. Y. Lin, F. Liu, E. Livshits, R. C. Lochan, A. Luenser, P. Manohar, S. F. Manzer, S.-P. Mao, N. Mardirossian, A. V. Marenich, S. A. Maurer, N. J. Mayhall, E. Neuscamman, C. M. Oana, R. Olivares-Amaya, D. P. O'Neill, J. A. Parkhill, T. M. Perrine, R. Peverati, A. Prociuk, D. R. Rehn, E. Rosta, N. J. Russ, S. M. Sharada, S. Sharma, D. W. Small, A. Sodt, T. Stein, D. Stück, Y.-C. Su, A. J. Thom, T. Tsuchimochi, V. Vanovschi, L. Vogt, O. Vydrov, T. Wang, M. A. Watson, J. Wenzel, A. White, C. F. Williams, J. Yang, S. Yeganeh, S. R. Yost, Z.-Q. You, I. Y. Zhang, X. Zhang, Y. Zhao, B. R. Brooks, G. K. Chan, D. M. Chipman, C. J. Cramer, W. A. Goddard III, M. S. Gordon, W. J. Hehre, A. Klamt, H. F. Schaefer III, M. W. Schmidt, C. D. Sherrill, D. G. Truhlar, A. Warshel, X. Xu, A. Aspuru-Guzik, R. Baer, A. T. Bell, N. A. Besley, J.-D. Chai, A. Dreuw, B. D. Dunietz, T. R. Furlani, S. R. Gwaltney, C.-P. Hsu, Y. Jung, J. Kong, D. S. Lambrecht, W. Liang, C. Ochsenfeld, V. A. Rassolov, L. V. Slipchenko, J. E. Subotnik, T. V. Voorhis, J. M. Herbert, A. I. Krylov, P. M. Gill and M. Head-Gordon, *Mol. Phys.*, 2015, **113**, 184–215.

41 M. Rivera, M. Dommett and R. Crespo-Otero, *J. Chem. Theory Comput.*, 2019, **15**, 2504–2516.

42 M. Rivera, M. Dommett, A. Sidat, W. Rahim and R. Crespo-Otero, *J. Comput. Chem.*, 2020, **41**, 1045–1058.

43 J. Schirmer, *Phys. Rev. A: At., Mol., Opt. Phys.*, 1982, **26**, 2395–2416.

44 A. B. Trofimov and J. Schirmer, *J. Phys. B: At., Mol. Opt. Phys.*, 1995, **28**, 2299.

45 B. Hourahine, B. Aradi, V. Blum, F. Bonafé, A. Buccheri, C. Camacho, C. Cevallos, M. Y. Deshaye, T. Dumitrica, A. Dominguez, S. Ehlert, M. Elstner, T. van der Heide, J. Hermann, S. Irle, J. J. Kranz, C. Köhler, T. Kowalczyk, T. Kubař, I. S. Lee, V. Lutsker, R. J. Maurer, S. K. Min, I. Mitchell, C. Negre, T. A. Niehaus, A. M. N. Niklasson, A. J. Page, A. Pecchia, G. Penazzi, M. P. Persson, J. Řezáč, C. G. Sánchez, M. Sternberg, M. Stöhr, F. Stuckenberg, A. Tkatchenko, V. W.-Z. Yu and T. Frauenheim, *J. Chem. Phys.*, 2020, **152**, 124101.

46 M. Elstner, D. Porezag, G. Jungnickel, J. Elsner, M. Haugk, T. Frauenheim, S. Suhai and G. Seifert, *Phys. Rev. B: Condens. Matter Mater. Phys.*, 1998, **58**, 7260–7268.

47 F. J. Hernández and R. Crespo-Otero, *Annu. Rev. Phys. Chem.*, 2023, **74**, 547–571.

48 J. Aragó and A. Troisi, *Phys. Rev. Lett.*, 2015, **114**, 1–5.

49 Z. Li, C. Roscini, R. Núñez, F. Teixidor, C. Viñas, E. Ruiz and J. G. Planas, *J. Mater. Chem. C*, 2024, **12**, 2101–2109.

50 L. Stojanović and R. Crespo-Otero, *ChemPhotoChem*, 2019, **3**, 907–915.

51 L. Stojanovic and R. Crespo-Otero, *Molecules*, 2022, **27**, 522.

52 L. Stojanović and R. Crespo-Otero, *J. Phys. Chem. C*, 2020, **124**, 17752–17761.

53 T. J. Penfold, F. B. Dias and A. P. Monkman, *Chem. Commun.*, 2018, **54**, 3926–3935.

54 J. Gibson and T. J. Penfold, *Phys. Chem. Chem. Phys.*, 2017, **19**, 8428–8434.

55 T. J. Penfold, E. Gindensperger, C. Daniel and C. M. Marian, *Chem. Rev.*, 2018, **118**, 6975–7025.

56 G. Herzberg and E. Teller, *Z. Phys. Chem.*, 1933, **21B**, 410–446.

57 J. M. Dos Santos, D. Hall, B. Basumatary, M. Bryden, D. Chen, P. Choudhary, T. Comerford, E. Crovini, A. Danos, J. De, S. Diesing, M. Fatahi, M. Griffin, A. K. Gupta, H. Hafeez, L. Hämmerling, E. Hanover, J. Haug, T. Heil, D. Karthik, S. Kumar, O. Lee, H. Li, F. Lucas, C. F. R. Mackenzie, A. Mariko, T. Matulaitis, F. Millward, Y. Olivier, Q. Qi, I. D. W. Samuel, N. Sharma, C. Si, L. Spierling, P. Sudhakar, D. Sun, E. Tankelevičiutė, M. Duarte Tonet, J. Wang, T. Wang, S. Wu, Y. Xu, L. Zhang and E. Zysman-Colman, *Chem. Rev.*, 2024, **124**, 13736–14110.